A bistable model for active domain formation on cell membranes

Master of Science
Physics of Complex Systems

Pascal Christopher Iuliano

Politecnico di Torino

Supervised by Prof. Andrea Gamba

Table of contents

Abstract 5

Introduction 7

Mean-field model 9

1 Model description 9
2 Open-loop system 11
3 Uniform steady states of the open-loop system 11
4 Closed-loop system 13
5 Relaxation of the closed-loop system to the steady state 14
6 Control parameters 18

Numerical model 19

1 Model description 19
2 Role of catalytic activity 19
3 Slowing down of coarsening in the symmetric case 22
4 Role of dissociation rates 24
5 Role of the total number of enzymes 27

Conclusions 33

Appendix A 35

Bibliography 37

Abstract

During the past decade, phase separation has emerged as a main driver of the self-organizing processes taking place in eukaryotic cells, whereby membranes and other biological components acquire specific chemical identities, corresponding to distinct biological functions. Most often, such processes are "active", i.e. they involve the action of energy-consuming enzymatic reactions. The aim of this thesis is to study a minimal model of active domain formation on cell membranes, combining an analytical approach and numerical computations. We derive a mean-field phase diagram identifying parameter regions where the membrane system tends to demix by either a nucleation process or by spinodal decomposition. Numerical simulations confirm the general structure of the mean-field diagram and allow to discuss some kinetic effects that cannot be captured in the mean-field approach.

Introduction

Phase separation is the process in which a homogeneous mixture of a number of molecular species spontaneously separates (demixes) in two coexisting phases characterized by different concentrations of one or more molecular species. During the past decade it has become increasingly clear that this phenomenon plays an important role in biology, as it participates in processes whereby, within eukaryotic cells, membranes and other biological components self-organize in different internal structures [1, 2, 3, 4]. These can emerge spontaneously or by means of specific driving factors inducing chains of symmetry-breaking events. For example, stem cells generate differentiated daughter cells by asymmetric cell division, a central process in the maintenance of living tissues, endowing them with specific fate determinants. Symmetry breaking takes place also in the presence of extracellular chemotactic gradients, that cause the cell to develop an advancing anterior part and a retracting posterior part endowed with different chemical compositions. Typically, these non equilibrium processes of internal organization require energy to sustain heterogeneity among the distinct phases, and are therefore termed as "active processes". The main aspect of phase separation in biological processes is that it allows to generate specific behaviors with specialized functionalities, for instance controlling RNA metabolism or DNA damage response, by spatially segregating proteins and nucleic acids in cells. This ordering of similar molecules in spatially separated domains is driven by a combination of attractive and repulsive interactions. Phase separation may take place abruptly when some control parameter crosses some critical value and a tipping point is reached. Here, we focus on phase separation processes taking place on cell membranes, where different types of lipids and membrane-bound molecules undergo transformations induced by enzymes that are constantly shuttling between the membrane and cytosol. We study in particular how specific molecular concentrations and reaction rates influence the phase separation process. It is observed that the separation into two different phases can occur either by nucleation or by spinodal decomposition. Nucleation takes place when a germ (droplet) of a stable phase is formed by thermal fluctuations in the "sea" of a metastable phase. Spinodal decomposition occurs when a homogeneous phase becomes thermodynamically unstable and fluctuations induce its decay into a stable phase simultaneously in all of the regions of the system. The problem is studied by combining a simple mean-field model, that can be treated analytically, and a numerical model that allows to observe kinetic features not captured by the mean-field.

Mean-field model

1 Model description

Here we describe a simple model for active phase separation on cell membranes, driven by positive feedback loops induced by the interactions between membrane-localized, laterally diffusing molecules and a finite pool of enzymes that shuttle between the membrane and cytosol. A similar model was initially introduced in Ref. [5] to describe chemotactic polarization. There, a single positive feedback loop was considered, and polarization was driven by an external activation field. Here we study in detail the process of spontaneous phase separation in a more symmetric model containing two positive feedback loops [6] when the external activation field is switched off.

On the membrane, we will consider the following concentration fields:

$$\begin{aligned} A &: \text{membrane-localized molecules} \\ B &: \text{modification of } A \\ E_A &: \text{enzyme that converts } B \to A \\ E_B &: \text{enzyme that converts } A \to B \end{aligned}$$

The E_A, E_B enzymes shuttle between membrane and cytosol. Binding of E_A to the membrane is favored by A, binding of E_B to the membrane is favored by B. These two interactions introduce two reinforcing feedback loops, favoring the formation of membrane regions enriched in either A and E_A, or B and E_B.

In the cytosol, the following concentration fields are considered:

$$\begin{aligned} E_A^{\text{cyto}} &: \text{cytosolic, freely diffusing form of } E_A \\ E_B^{\text{cyto}} &: \text{cytosolic, freely diffusing form of } E_B \end{aligned}$$

To simplify the model, the following assumptions are made:

- diffusion in the cytosol is much faster than lateral diffusion on the membrane: the limit of infinite cytosolic diffusion is thus considered, and the cytosol is treated as an unstructured reservoir (the fields E_A^{cyto} and E_B^{cyto} are therefore treated as numbers);
- the production and destruction of the membrane-localized molecules A and B are neglected, and only the interconversion processes $A \to B$ and $B \to A$ are considered, therefore $A + B = c = \text{const}$.

The chemical kinetics of the above species can be described in a mean-field (mass-action kinetic) approach as (see Fig. 1):

$$\frac{\partial A}{\partial t} = D\,\Delta A - g(A, B, E_A, E_B) \tag{1}$$

$$\frac{\partial B}{\partial t} = D\,\Delta B + g(A, B, E_A, E_B) \tag{2}$$

$$g(A, B, E_A, E_B) = k_B^c \frac{E_B\, A}{K + A} - k_A^c \frac{E_A\, B}{K + B} \tag{3}$$

$$\frac{\partial E_A}{\partial t} = k_A^a\, E_A^{\text{cyto}}\, A - k_A^d\, E_A \tag{4}$$

$$\frac{\partial E_B}{\partial t} = k_B^a\, E_B^{\text{cyto}}\, B - k_B^d\, E_B \tag{5}$$

where Michaelis-Menten terms (for simplicity, with the same Michaelis-Menten constant K) are adopted to describe the enzymatic kinetics, the reaction term g describes the enzyme-driven interconversion of A and B, and Δ is the Laplace-Beltrami operator on the curved membrane surface [6]. In what follows, we will mainly analyze model (1–5) as a set of deterministic equations. However, we will also assume the presence of additive noise terms when discussing nucleation phenomena.

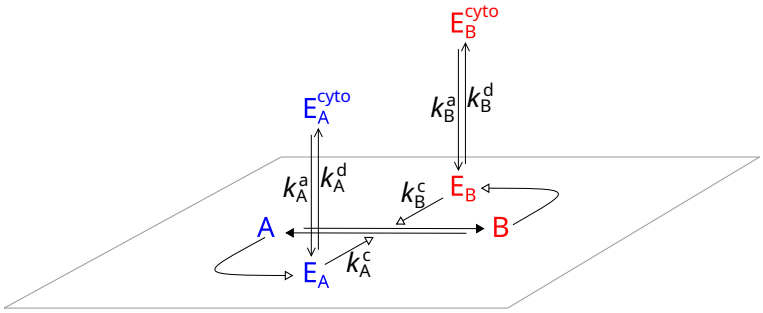

Figure 1. Minimal model of active domain formation.

If $A+B$ is uniformly distributed at initial time, adding (1) and (2) shows that the following conservation law holds at all times:

$$A+B \;=\; c \;=\; \text{const} \tag{6}$$

The total number of enzymes shuttling between the membrane and the cytosol is conserved:

$$\theta\,\langle E\rangle + E^{\text{cyto}} \;=\; E^{\text{tot}} \tag{7}$$

where $\theta = \mathcal{S}\,/\,\mathcal{V}$, $\mathcal{S}$ is the membrane surface, $\mathcal{V}$ is the volume of the cytosolic reservoir that exchanges enzymes with $\mathcal{S}$ and $\langle E\rangle$ represents the average value of the membrane-bound molecule E on the membrane:

$$\langle E\rangle \;=\; \frac{1}{\mathcal{S}}\int E\,\mathrm{d}\sigma$$

If association/dissociation of E_A and E_B to/from the membrane is much faster than the typical dynamics of the A and B fields on the membrane, one may consider the E_A and E_B fields to be in approximate equilibrium with A and B:

$$E_A \;=\; \frac{E_A^{\text{cyto}}}{K_A^d}\,A \tag{8}$$

$$E_B \;=\; \frac{E_B^{\text{cyto}}}{K_B^d}\,B \tag{9}$$

where the dissociation constants $K_A^d = k_A^d\,/\,k_A^a$, $K_B^d = k_B^d\,/\,k_B^a$ were used. Moreover, using (7) one may reexpress:

$$E_A^{\text{cyto}} \;=\; \frac{E_A^{\text{tot}}}{1+\theta\,\langle A\rangle\,/\,K_A^d} \tag{10}$$

$$E_B^{\text{cyto}} \;=\; \frac{E_B^{\text{tot}}}{1+\theta\,\langle B\rangle\,/\,K_B^d} \tag{11}$$

The conservation law (6) allows to rewrite the system dynamics in terms of the single order parameter

$$\phi \;=\; B-A \tag{12}$$

obeying the constrained Landau-Ginzburg equation

$$\frac{\partial\phi}{\partial t} \;=\; D\,\Delta\phi + f_{\alpha,\beta}(\phi) \tag{13}$$

where

$$f_{\alpha,\beta}(\phi) \;=\; (c^2-\phi^2)\,[\beta\,h(-\phi)-\alpha\,h(\phi)], \quad \text{with} \quad h(\phi) \;=\; \frac{1}{2\,K+c-\phi} \tag{14}$$

and

$$\alpha \;=\; \frac{k_A^c\,E_A^{\text{tot}}}{K_A^d+(c-\langle\phi\rangle)\,\theta\,/\,2}, \quad \beta \;=\; \frac{k_B^c\,E_B^{\text{tot}}}{K_B^d+(c+\langle\phi\rangle)\,\theta\,/\,2} \tag{15}$$

Observe that α and β are functional integrals of the field configuration ϕ. In particular, α is an increasing function of $\langle\phi\rangle$ and β is a decreasing function of $\langle\phi\rangle$. This reflects the fact that the shuttling of E_A and E_B enzymes from the cytosol to the membrane regions occupied, respectively, by the A and the B molecules, introduces in the system a *global negative feedback*: the E_A enzymes promote the spread of the A membrane region and the binding of new E_A enzymes to it but, at the same time, E_A enzymes are depleted from the cytosol and the propensity of their binding to A region decreases. The opposite happens with the E_B enzymes. We will show in the following Sections that this global negative feedback favors the formation of stable steady states characterized by the spatial coexistence of membrane regions occupied by the A phase with regions occupied by the B phase.

2 Open-loop system

We start the analysis of the problem (13,14) by treating α and β as assigned constants. In this case, (13) can be rewritten in the variational form

$$\frac{\partial\phi}{\partial t} \;=\; D\,\Delta\phi - V'_{\alpha,\beta}(\phi) \;=\; -\frac{\delta\mathcal{F}_{\alpha,\beta}}{\delta\phi} \tag{16}$$

in terms of the effective energy

$$\mathcal{F}_{\alpha,\beta}[\phi] \;=\; \int\left[\frac{D}{2}\,(\nabla\phi)^2 + V_{\alpha,\beta}(\phi)\right]\mathrm{d}\sigma \tag{17}$$

where the potential

$$V_{\alpha,\beta}(\phi) \;=\; -\int f_{\alpha,\beta}(\phi)\,\mathrm{d}\phi \tag{18}$$

can be written explicitly using

$$\int\frac{c^2-\phi^2}{2\,K+c\pm\phi}\,\mathrm{d}\phi \;=\; \mp\frac{\phi^2}{2} + (2\,K+c)\,\phi \mp 4\,K\,(K+c)\log(2\,K+c\pm\phi) + \mathrm{const} \tag{19}$$

3 Uniform steady states of the open-loop system

Uniform equilibrium solutions of (16) correspond to the roots of the equation $f_{\alpha,\beta}(\phi)=0$, which are readily found from (14) to be

$$\phi_- \;=\; -c, \qquad \phi_0 \;=\; (2\,\kappa+1)\,\frac{1-\rho}{1+\rho}\,c, \qquad \phi_+ \;=\; c \tag{20}$$

where

$$\rho \;=\; \beta/\alpha, \qquad \kappa \;=\; K/c \tag{21}$$

The combination of (6,12) implies that acceptable roots ϕ must satisfy the condition

$$-c \;\leqslant\; \phi \;\leqslant\; c \tag{22}$$

In particular, ϕ_0 satisfies (22) if and only if

$$\frac{\kappa}{1+\kappa} \;\leqslant\; \rho \;\leqslant\; \frac{1+\kappa}{\kappa} \tag{23}$$

Stable roots satisfy $V''_{\alpha,\beta}=-f'_{\alpha,\beta}>0$. By an elementary study of the sign of $f_{\alpha,\beta}$ one obtains the picture summarized in Table 1.

$\rho<\frac{\kappa}{1+\kappa}$	$\phi_0>c$	ϕ_- stable, ϕ_+ unstable	$\mathrm{A_m}$
$\frac{\kappa}{1+\kappa}\leqslant\rho\leqslant\frac{1+\kappa}{\kappa}$	$-c\leqslant\phi_0\leqslant c$	ϕ_-, ϕ_+ stable, ϕ_0 unstable	$\mathrm{A_b}$, C, $\mathrm{B_b}$
$\rho>\frac{1+\kappa}{\kappa}$	$\phi_0<-c$	ϕ_- unstable, ϕ_+ stable	$\mathrm{B_m}$

Table 1. Stability of uniform equilibria. The $\mathrm{A_m}$ and $\mathrm{B_m}$ cases correspond to monostable equilibria where, respectively, the A or the B phase is favored. In the bistable case, the subcases $\rho<1$ ($\mathrm{A_b}$), $\rho=1$ (C), and $\rho>1$ ($\mathrm{B_b}$) can be distinguished.

The corresponding shapes of $f_{\alpha.\beta}(\phi)$ and of the potential $V_{\alpha.\beta}(\phi)$ are shown in Fig. 2 and Fig. 3 respectively. The A_b, C, and B_b bistable cases are separately analyzed in the lowest rows of the two Figures.

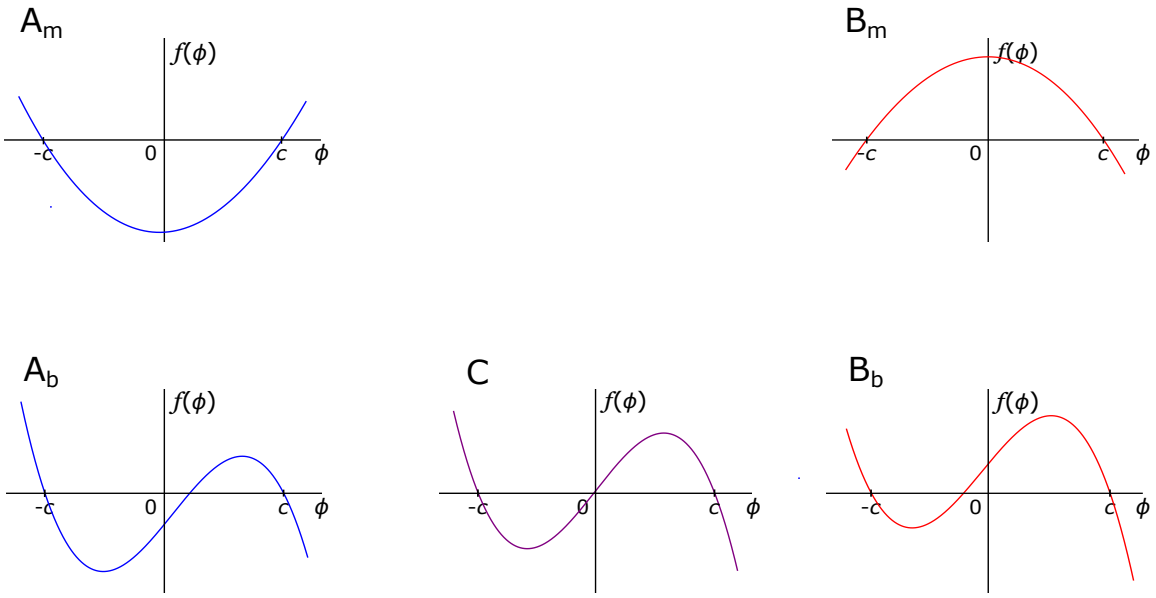

Figure 2. Shapes of the function $f_{\alpha.\beta}(\phi)$ for the cases listed in Table 1. Blue: A phase is favored. Red: B phase is favored. Purple: phase coexistence.

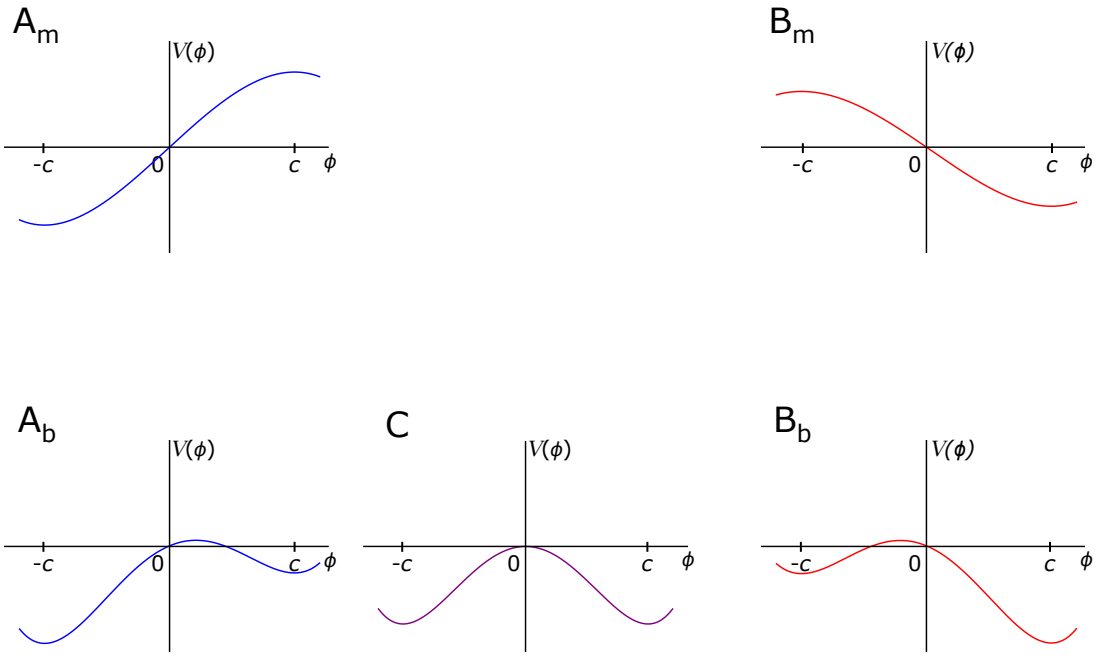

Figure 3. Shapes of the potential $V_{\alpha.\beta}(\phi)$ for the cases listed in Table 1. Blue: A phase is favored. Red: B phase is favored. Purple: phase coexistence.

In the A_b, C, and B_b cases, two stable equilibria are possible. Either the A phase or the B phase are favored, depending on the sign of the *degree of metastability*

$$\Delta V_{\alpha,\beta} \;=\; V_{\alpha,\beta}(\phi_+) - V_{\alpha,\beta}(\phi_-) \;=\; (\alpha-\beta)\int_{-c}^{c}(c^2-\phi^2)\,h(\phi)\mathrm{d}\phi \tag{24}$$

showing that the three cases correspond to the parametric conditions listed in Table 2.

$\rho<1$	$\alpha>\beta$	$\Delta V_{\alpha,\beta}>0$	A phase is favored	$\mathrm{A_b}$
$\rho=1$	$\alpha=\beta$	$\Delta V_{\alpha,\beta}=0$	phase coexistence	C
$\rho>1$	$\alpha<\beta$	$\Delta V_{\alpha,\beta}<0$	B phase is favored	$\mathrm{B_b}$

Table 2. Parameter ranges corresponding to each of the bistable cases $\mathrm{A_b}$, C and $\mathrm{B_b}$.

One of the parameters controlling phase separation is the barrier that separates the two potential wells of $V_{\alpha,\beta}(\phi)$. For $\alpha=\beta$, this is

$$b \;=\; V_{\alpha,\beta}(\phi_0) - V_{\alpha,\beta}(\phi_-) \;=\; \alpha\left[c^2 + 4\,K\,(K+c)\log\left(1+\frac{c^2}{4\,K^2+4K\,c}\right)\right] \tag{25}$$

4 Closed-loop system

Let us now study the constraints on generic configurations of ϕ due to the ϕ dependence of α, β. From (15, 21) we get

$$\rho \;=\; \frac{\beta}{\alpha} \;=\; \frac{k_{\mathrm{B}}^{\mathrm{c}}\,k_{\mathrm{B}}^{\mathrm{a}}\,k_{\mathrm{A}}^{\mathrm{d}}\,E_B^{\mathrm{tot}}}{k_{\mathrm{A}}^{\mathrm{c}}\,k_{\mathrm{A}}^{\mathrm{a}}\,k_{\mathrm{B}}^{\mathrm{d}}\,E_{\mathrm{A}}^{\mathrm{tot}}}\,\frac{1+(c-\langle\phi\rangle)\,\theta/2K_A^d}{1+(c+\langle\phi\rangle)\,\theta/2K_B^d} \tag{26}$$

Observe that ρ is a decreasing function of $\langle\phi\rangle$. This is again a manifestation of the global negative feedback mechanism described at the end of the Sect. 1.

Eq. 26 can be solved to give

$$\langle\varphi\rangle \;=\; \frac{(1+\rho_A)\,\rho_1-(1+\rho_B)\,\rho}{\rho_A\,\rho_1+\rho_B\,\rho} \tag{27}$$

where for convenience we introduce the following new parameter combinations and dimensionless quantities:

$$\rho_0 \;=\; \frac{k_{\mathrm{B}}^{\mathrm{c}}\,E_{\mathrm{B}}^{\mathrm{tot}}}{k_{\mathrm{A}}^{\mathrm{c}}\,E_{\mathrm{A}}^{\mathrm{tot}}},\quad \rho_1 \;=\; \frac{K_{\mathrm{A}}^{\mathrm{d}}}{K_{\mathrm{B}}^{\mathrm{d}}}\,\rho_0,\quad \mathscr{c} \;=\; \theta\,c,\quad \rho_A \;=\; \frac{\mathscr{c}}{2\,K_A^d},\quad \rho_B \;=\; \frac{\mathscr{c}}{2\,K_B^d},\quad \varphi \;=\; \phi/c \tag{28}$$

It is important to observe that $\langle\varphi\rangle$ is not free to assume any possible value, but it is constrained by the "physical" condition

$$-1 \;\leqslant\; \langle\varphi\rangle \;\leqslant\; 1$$

which, using (27), translates into

$$\rho_0/\rho_+ \;\leqslant\; \rho \;\leqslant\; \rho_0/\rho_- \tag{29}$$

with

$$\rho_- \;=\; \frac{K_B^d}{K_A^d+\mathscr{c}},\quad \rho_+ \;=\; \frac{K_B^d+\mathscr{c}}{K_{\mathrm{A}}^{\mathrm{d}}} \tag{30}$$

The *right* boundary corresponds to $\langle\varphi\rangle=-1$ (again consequence of the negative feedback mechanism), a homogeneous distribution of *uniform* A phase, while the *left* boundary corresponds to $\langle\varphi\rangle=+1$, a homogeneous distribution of *uniform* B phase.

Fig. 4 summarizes our findings. Regions $\mathrm{A_m}$, $\mathrm{A_b}$ are separated from $\mathrm{B_m}$, $\mathrm{B_b}$ by the coexistence line C ($\rho=1$). The only physically realizable values of ρ are those in the strip $\rho_0/\rho_+\leqslant\rho\leqslant\rho_0/\rho_-$, marked with darker colors in the diagram. The equations of the lines delimiting the different regions are summarized in Table 3.

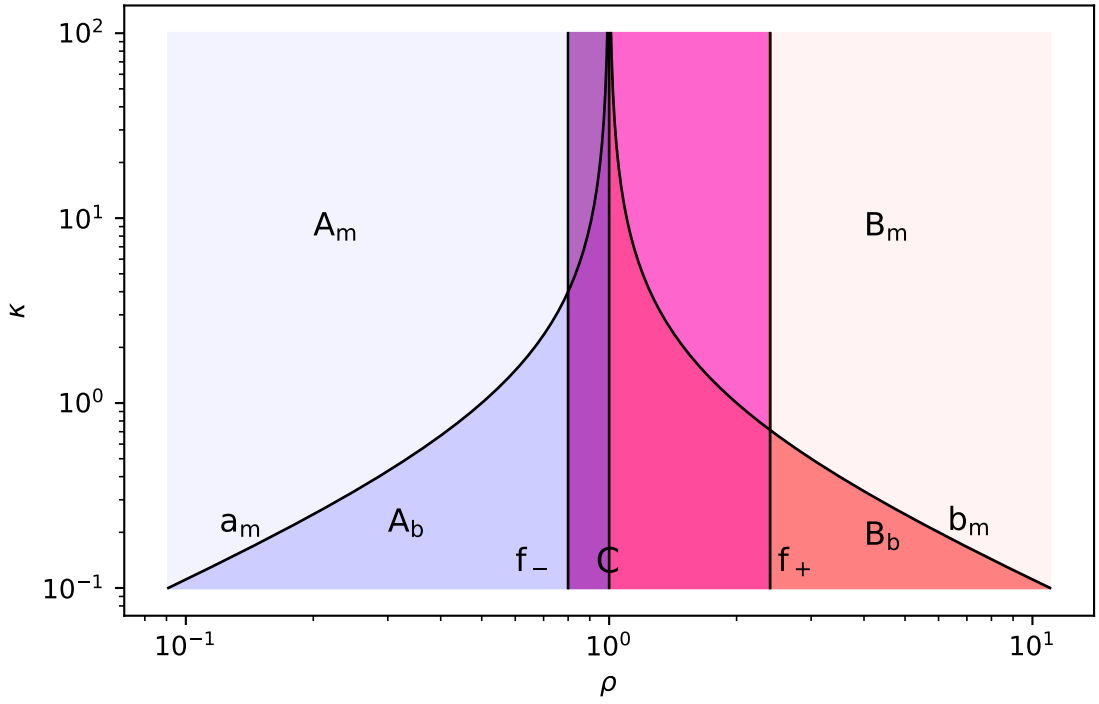

Figure 4. Parameter regions corresponding to A-dominated monostable (light blue) and bistable (blue) cases, or B-dominated monostable (light red) and bistable (red) cases. The only physically realizable values of ρ are those in the central strip colored with different shades of purple (see Eq. 29). The diagram was obtained with K_A^d=2, K_B^d=1 and c=1.

lines	equations
C	$\rho = 1$
a_m	$\rho = \frac{\kappa}{1+\kappa}$
b_m	$\rho = \frac{1+\kappa}{\kappa}$
f_-	$\rho = \rho_0 / \rho_+$
f_+	$\rho = \rho_0 / \rho_-$

Table 3. Equations of the curves delimiting the various regions in the diagram of Fig. 4.

Fig. 4 shows that the bistable region is larger for smaller values of κ ($c \gg K$), i.e. in the saturation regime of Michaelis-Menten kinetics (see App. A), and smaller for larger values of κ ($c \ll K$), i.e. in the linear regime. Therefore, the strength of the effective interaction between the chemical components of the system, responsible for the process of phase separation, can be assumed to be proportional to c/K. This is coherent with the idea that the membrane-localized molecules A, B mediate an effective interaction between the enzyme species E_A, E_B.

5 Relaxation of the closed-loop system to the steady state

To a given initial configuration of ϕ there corresponds a representative point in the physical strip $\rho_0/\rho_+ \leqslant \rho \leqslant \rho_0/\rho_-$ (see Eq. 29 and Fig. 4). We will now show that the ϕ dynamics described by the constrained Landau-Ginzburg system (13–15) induces a drift of the representative value ρ towards the coexistence line $\rho = 1$.

Let us first focus on the $\rho < 1$ ($\beta < \alpha$) part of the diagram, where the A phase is favored (see Tab. 2). In this part of the diagram, let us consider a representative value ρ, corresponding to a generic configuration where the regions occupied by A phase are separated by some interface from

regions occupied by the B phase. Since the A phase is favored, the regions occupied by the A phase will tend to grow at the expense of the regions occupied by the B phase, so that $\langle\phi\rangle = \langle B\rangle - \langle A\rangle$ will decrease, and consequently (due to (15)) α will decrease and β will increase. Summarizing:

$$\rho<1: \qquad \beta<\alpha, \qquad \frac{\partial\alpha}{\partial t} \;<\; 0, \qquad \frac{\partial\beta}{\partial t}>0$$

which together imply

$$\frac{\partial\rho}{\partial t} \;=\; \frac{\partial}{\partial t}\frac{\beta}{\alpha} \;=\; \frac{1}{\alpha}\left(\frac{\partial\beta}{\partial t}-\frac{\beta}{\alpha}\frac{\partial\alpha}{\partial t}\right) \;>\; \frac{1}{\alpha}\left(\frac{\partial\beta}{\partial t}-\frac{\partial\alpha}{\partial t}\right) \;>\; 0$$

and also (using (24))

$$\frac{\partial}{\partial t}\Delta V_{\alpha,\beta} \;<\; 0$$

which shows again the effects of the *negative feedback* [6]: the more the A phase grows, the less favored its further expansion becomes, since the *degree of metastability* (24) decreases. Consequently, the growth of the phase slows down as time advances [6].

The opposite situation is verified in the $\rho>1$ part of the diagram:

$$\rho>1: \qquad \beta>\alpha, \qquad \frac{\partial\alpha}{\partial t} \;>\; 0, \qquad \frac{\partial\beta}{\partial t}<0, \qquad \frac{\partial\rho}{\partial t}<0, \qquad \frac{\partial}{\partial t}\Delta V_{\alpha,\beta}>0$$

In both cases the depth of the two potential wells of $V(\phi)$ tends to be equalized, and the system tends to the coexistence line $\rho=1$, where $\alpha=\beta$, $\phi_0=0$, $f_{\alpha,\beta}(-\phi)=-f_{\alpha,\beta}(\phi)$ and $V(-\phi)=-V(\phi)$. At the same time, $\langle\phi\rangle$ tends to the equilibrium value (cf. (27))

$$\langle\phi\rangle_{\rm eq} \;=\; \frac{(1+\rho_A)\,\rho_1-(1+\rho_B)}{\rho_A\,\rho_1+\rho_B}\,c$$

and the last stages of the dynamics are well described by the Landau-Ginzburg equation (16) with the corresponding asymptotic values of $\alpha=\beta$ and approximate global "mass" conservation

$$\langle\phi\rangle \;\simeq\; \langle\phi\rangle_{\rm eq}$$

In the presence of additive noise, a phase-separated state may originate from a uniform field configuration ϕ by either a spinodal decomposition (if the representative point of the system is initially in the part $\mathrm{A_m}$ or $\mathrm{B_m}$ of the diagram) or by nucleation (if the representative point of the system is initially in the part $\mathrm{A_b}$ or $\mathrm{B_b}$ of the diagram).

To study the approach to the steady state it is convenient to imagine that the system is prepared in one of the uniquely defined uniform states corresponding to points of one of the two boundaries of the physical strip $\rho_0/\rho_+ \leqslant \rho \leqslant \rho_0/\rho_-$ (see Eq. 29 and Fig. 4), i.e. ether $\varphi=-1$ (right boundary) or $\varphi=+1$ (left boundary). Then, different situations are possible, depending on whether the strip lies to the left or to the right of the coexistence line $\rho=1$, or whether the coexistence line $\rho=1$ is contained in the strip itself.

When the strip lies to the left of the coexistence line $\rho=1$ (Fig. 5, left column), at the steady state there will be a uniform A phase, since, even if the system is prepared on the left boundary of the strip (pure B phase), the negative feedback will drive it towards the right boundary ($\varphi=-1$, pure A phase). The same would be true if the system was prepared in any other uniform or non-uniform state, corresponding to a representative point contained in the interior of the strip. Moreover, the transition from an initial uniform B phase to the steady state A phase takes place either by spinodal decomposition, if the system is initially in the monostable (Fig. 4, $\mathrm{A_m}$) region (Fig. 5, $\mathrm{A_s}$, $\mathrm{A_{s'}}$), or by nucleation, if the representative point is initially in the bistable (Fig. 4, $\mathrm{A_b}$) region (Fig. 5, $\mathrm{A_n}$). The opposite happens when the strip lies to the right of the coexistence line $\rho=1$ (Fig. 5, right column), leading to the $\mathrm{B_s}$, $\mathrm{B_{s'}}$, $\mathrm{B_n}$ cases of Fig. 5.

When the coexistence line $\rho=1$ is instead contained in the interior of the physical strip (Fig. 5, center column), the steady state will always be characterized by *phase coexistence*, since the negative feedback will always drive the system towards the coexistence line $\rho=1$. Translating the geometric condition on the relative position of the strip (see Eq. 29) with respect to the coexistence line $\rho=1$, one finds that phase coexistence is reached at the steady state only if

$$\rho_- \;\leqslant\; \rho_0 \;\leqslant\; \rho_+ \tag{31}$$

Interestingly, the width of the bistability region (30) does not depend on κ:

$$\rho_+ - \rho_- \;=\; \frac{(K_B^d + c)\,(K_A^d + c) - K_A^d\,K_B^d}{K_A^d\,(K_A^d + c)} \;\geqslant\; 0$$

The value of $\langle\varphi\rangle$ in the steady state is given by

$$\langle\varphi\rangle_{\rm eq} \;=\; \begin{cases} -1 & , \;\; \rho_0 \,<\, \rho_- \\ \dfrac{(1 + 2\,K_A^d/c)\,\rho_0 - (1 + 2\,K_B^d/c)}{\rho_0 + 1} & , \;\; \rho_- \,<\, \rho_0 \,<\, \rho_+ \\ +1 & , \;\; \rho_0 \,>\, \rho_+ \end{cases}$$

Phase coexistence configurations are characterized by regions of the A phase separated from regions of the B phase by a phase interface. In the limit of thin interface (small diffusivity) the fraction of membrane occupied by the B phase is approximately equal to $\frac{1}{2}\,(1 + \langle\varphi\rangle_{\rm eq})$.

The transition from an initial uniform B phase to the steady phase coexistence state takes place either by spinodal decomposition (Fig. 5, $\mathrm{C_{ss}}$, $\mathrm{C_{sn}}$) or by nucleation (Fig. 5, $\mathrm{C_{ns}}$, $\mathrm{C_{nn}}$).

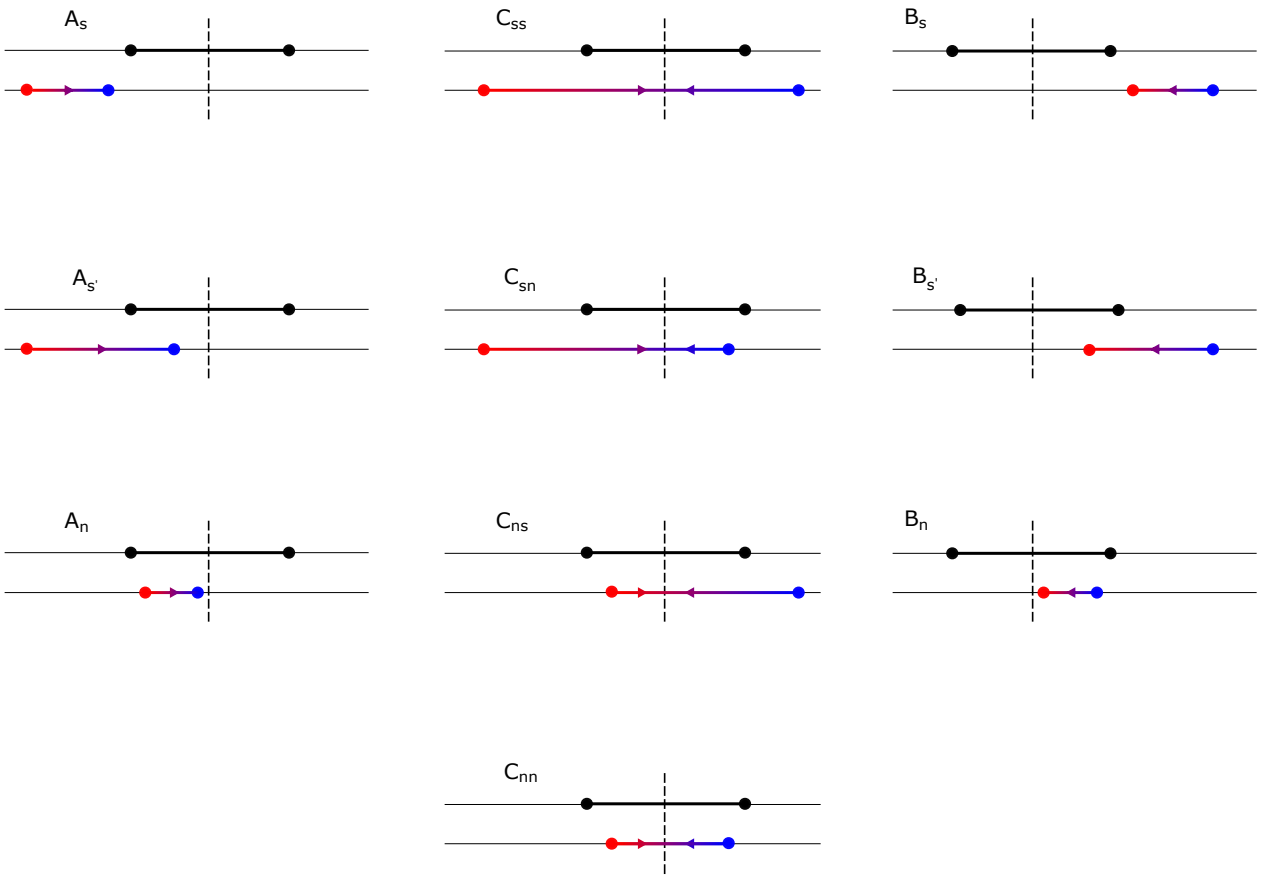

Figure 5. Classification of the paths of relaxation to the steady state. The graphs show the possible relative positions of the relevant intervals of ρ values, for fixed κ. Vertical dashed lines: $\rho = 1$. Black intervals: bistability region (see Eq. 23). Colored intervals: physical region (see Eq. 29). Red: B phase. Blue: A phase. The global negative feedback drives the system in the direction of the arrows. The A, B, C cases correspond to steady states characterized by a pure A phase, a pure B phase, or phase coexistence, respectively. Subscripts label different paths of approach to the steady state: nucleation (n), spinodal decomposition (s) or a combination of the two (s').

The parametric equations for the cases shown in Fig. 5 are listed in Table 4. The corresponding

regions of parameter space are shown in the phase diagram of Fig. 6.

A_s	$\rho_0 < \frac{\kappa}{1+\kappa}\,\rho_-$
$A_{s'}$	$\frac{\kappa}{1+\kappa}\,\rho_- < \rho_0 < \min\left(\rho_-, \frac{\kappa}{1+\kappa}\,\rho_+\right)$
A_n	$\frac{\kappa}{1+\kappa}\,\rho_+ < \rho_0 < \rho_-$
C_{ss}	$\frac{1+\kappa}{\kappa}\,\rho_- < \rho_0 < \frac{\kappa}{1+\kappa}\,\rho_+$
C_{sn}	$\rho_- < \rho_0 < \min\left(\frac{1+\kappa}{\kappa}\,\rho_-, \frac{\kappa}{1+\kappa}\,\rho_+\right)$
C_{ns}	$\max\left(\frac{1+\kappa}{\kappa}\,\rho_-, \frac{\kappa}{1+\kappa}\,\rho_+\right) < \rho_0 < \rho_+$
C_{nn}	$\max\left(\rho_-, \frac{\kappa}{1+\kappa}\,\rho_+\right) < \rho_0 < \min\left(\rho_+, \frac{1+\kappa}{\kappa}\,\rho_-\right)$
B_s	$\rho_0 > \frac{1+\kappa}{\kappa}\,\rho_+$
$B_{s'}$	$\max\left(\rho_+, \frac{1+\kappa}{\kappa}\,\rho_-\right) < \rho_0 < \frac{1+\kappa}{\kappa}\,\rho_+$
B_n	$\rho_+ < \rho_0 < \frac{1+\kappa}{\kappa}\,\rho_-$

Table 4. Parametric equations for the regions of the phase diagram shown in the following Fig. 6. In the A, B, C cases the final steady state is characterized, respectively, by a uniform A phase, a uniform B phase, or phase coexistence. The subscripts denote different modes of approach to the steady state: spinodal decomposition (s) or nucleation (n). The subscript s' denotes a mixed case where phase separation is initiated by a spinodal decomposition, but later on, the negative feedback drives the system in the nucleation region. Double subscripts are used when a different mode is followed, depending on whether the system is initially on the left or the right boundary of the physical strip (Eq. 29). See Eq. (30) for the definition of ρ_- and ρ_+.

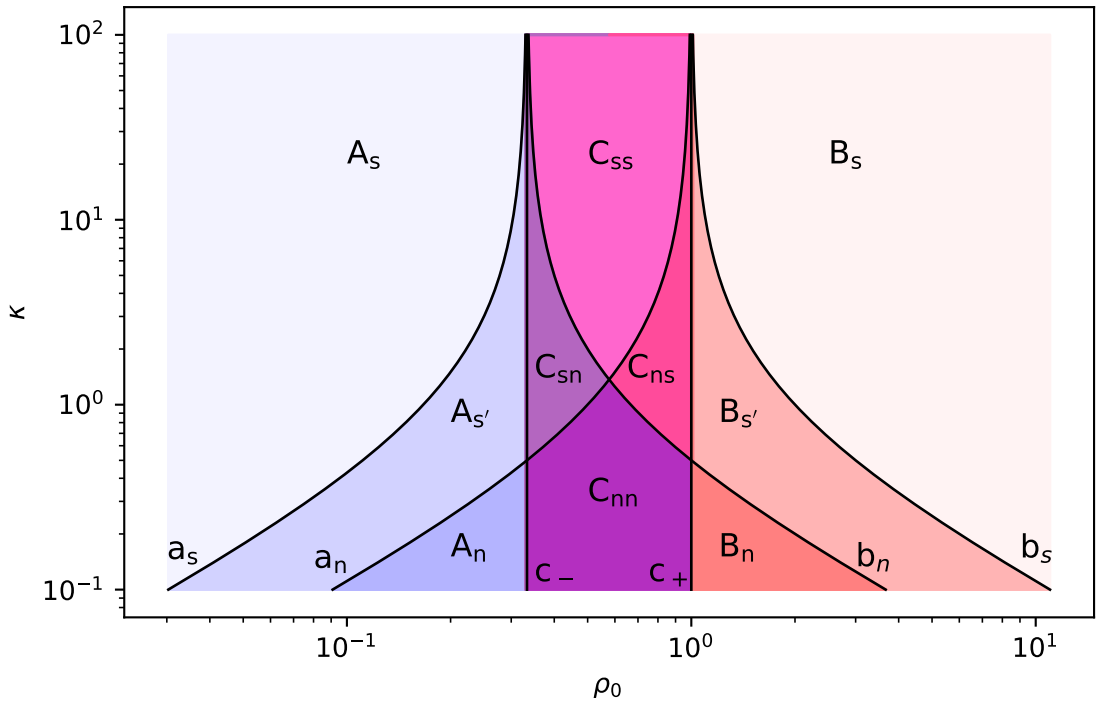

Figure 6. Phase diagram of the mean field model obtained with (13–15), obtained with K_A^d=2, K_B^d=1 and e=1. The equations of the lines delimiting the different regions are summarized in Table 5.

lines	equations
a_s	$\rho_0 = \frac{\kappa}{1+\kappa}\rho_-$
a_n	$\rho_0 = \frac{\kappa}{1+\kappa}\rho_+$
c_-	$\rho_0 = \rho_-$
c_+	$\rho_0 = \rho_+$
b_n	$\rho_0 = \frac{1+\kappa}{\kappa}\rho_-$
b_s	$\rho_0 = \frac{1+\kappa}{\kappa}\rho_+$

Table 5. Equations of the curves delimiting the various regions in the phase diagram of Fig. 6. See Eq. 30 for the definition of ρ_- and ρ_+.

6 Control parameters

The ρ_-, ρ_+ parameters (Eq. 30) control the extension of the coexistence region, while the κ parameter controls the mode of initiation of the phase separation process (spinodal decomposition or nucleation, see Table 4).

The expression

$$\frac{\rho_+}{\rho_-} = \left(1+\frac{c}{K_A^d}\right)\left(1+\frac{c}{K_B^d}\right)$$

shows that a large coexistence region is obtained when $c \gg K_A^d$, or $c \gg K_B^d$, or both. Recalling Eq. 28, and assuming for simplicity $K_A^d \sim K_B^d \sim K^d$, this condition can be rewritten as

$$c \gg \frac{\mathcal{V}}{\mathcal{S}} K^d \tag{32}$$

where $\mathcal{S}$ is the membrane surface and $\mathcal{V}$ is the volume of the cytosolic reservoir. Interestingly, Eq. 32 suggests that *in the presence of comparable surface concentrations c of membrane-bound molecules, phase separation should be favored on larger membrane bodies*.

Let us now analyze the role of the κ parameter. Fig. 6 shows that nucleation is favored for values of κ below the intersection of the a_n and b_n lines, i.e. for

$$\frac{\mathcal{V}}{\mathcal{S}} K^d > K \tag{33}$$

If both (32) and (33) are verified, phase coexistence states are expected to easily emerge from initial uniform state by a nucleation process, and $c \gg K$, corresponding to saturation regime of Michaelis-Menten kinetics.

Numerical model

1 Model description

In the present Section we provide a lattice-gas model implementation of the abstract model defined in Sect. 1 and explore the space of model parameters by way of numerical simulations. As a model of cell membrane, we consider a two-dimensional $L \times L$ square lattice with periodic boundary conditions in which each site can be occupied by either a single, free A or B molecule (states A, B), or a single A or B molecule bound to the corresponding E_A or E_B enzyme (states $A^\star$, $B^\star$). As a model of the cytosol, we consider an unstructured reservoir containing a number n_A, n_B of free enzymes of type E_A, E_B, respectively. Association of E_A and E_B enzymes to an A or B molecule on the membrane takes place with rates $r_A^a\, n_A$ and $r_B^a\, n_B$, respectively. Dissociation from an A or B molecule takes place with rates r_A^d and r_B^d, respectively. Moreover, a bound enzyme $A^\star$ or $B^\star$ induces the transition of a neighboring B or A molecule to the opposite A or B state with rate r_A^c, r_B^c, respectively. Simulations were performed applying Gillespie's algorithm [7] on an $L = 100$ lattice.

We expect the relation between the parameters of the lattice model and those of the mean-field theory of Sect. 1 to be non trivial. However, simple dimensional arguments suggest the rough estimates:

$$k_A^a \sim r_A^a\, \mathcal{V}, \qquad k_B^a \sim r_B^a\, \mathcal{V} \tag{1}$$

$$k_A^d \sim r_A^d, \qquad k_B^d \sim r_B^d \tag{2}$$

$$K_A^d \sim \frac{1}{\mathcal{V}}\frac{r_A^d}{r_A^a}, \qquad K_B^d \sim \frac{1}{\mathcal{V}}\frac{r_B^d}{r_B^a}, \qquad \kappa \sim K \sim K_A^d \sim K_B^d \tag{3}$$

$$\rho_0 = \frac{k_{\mathrm{B}}^{\mathrm{c}}\, E_{\mathrm{B}}^{\mathrm{tot}}}{k_{\mathrm{A}}^{\mathrm{c}}\, E_{\mathrm{A}}^{\mathrm{tot}}} \sim \frac{r_{\mathrm{B}}^{\mathrm{c}}\, n_{\mathrm{B}}^{\mathrm{tot}}}{r_{\mathrm{A}}^{\mathrm{c}}\, n_{\mathrm{A}}^{\mathrm{tot}}} \equiv \rho_0' \tag{4}$$

$$\rho_- \sim \frac{r_B^d/r_B^a}{r_A^d/r_A^a + L^2}, \qquad \rho_+ \sim \frac{r_B^d/r_B^a + L^2}{r_A^d/r_A^a} \tag{5}$$

$$\mathcal{S}c \sim L^2 \tag{6}$$

2 Role of catalytic activity

In this Section we report the results of simulations performed with varying values of r_A^c, r_B^c to study the dependence of the steady state on catalytic rates. All of the other parameter values were kept constant and had the same values for the A and B species (see Tables 1–4 below). For these values, the estimates (1–6) give $\kappa \sim 10^{-4}$, $\rho_- \sim 10^{-2}$, $\rho_+ \sim 10^2$. When $r_B^c < r_A^c$ (and therefore the A phase was favored) the sites of the system were initially mostly occupied by B molecules, except for a 10% randomly chosen sites occupied by A molecules, to allow the nucleation of regions of the A phase. The opposite choice was adopted when $r_B^c > r_A^c$. In both cases, free enzymes rapidly

bound to the membrane, leading to the formation of an A phase where sites were either in an A or an $A^\star$ state, and B phase where sites were either in a B or a $B^\star$ state. A slower evolution of the A phase and B phase regions characterized the later relaxation towards the statistical stationary state. In the snapshots of the simulations below, the A, $A^\star$, B and $B^\star$ states are shown in cyan, blue, pink and red, respectively.

When $r_B^c \ll r_A^c$ (see Fig. 1 and Table. 1), an initial mixture of the A and B phase nucleated larger and larger regions of the A phase, ultimately relaxing to a uniform A phase, in qualitative agreement with the prediction of the mean-field model.

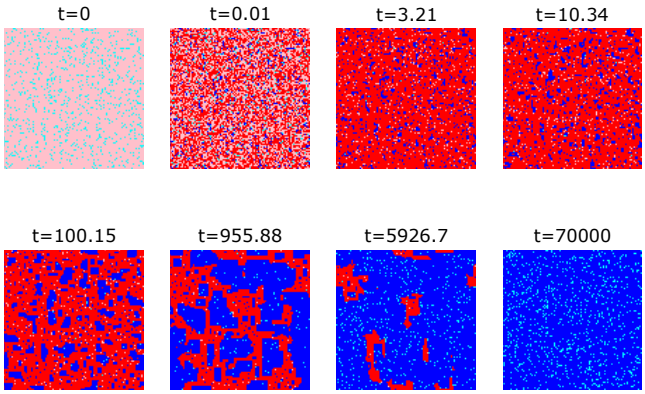

Figure 1. Emergence of a uniform A phase from a B-dominated random mixture of the A and B phases.

	A	B
r^a	0.01	0.01
r^d	1	1
r^c	100000	0.01
n^{tot}	10000	10000

Table 1. Rate constants and total number of enzymes of the two species for the simulation shown in Fig. 1 ($\rho_0' = 10^{-7}$).

By exchanging the parameters for the A and B species one observes a mirror behavior (see Fig. 2).

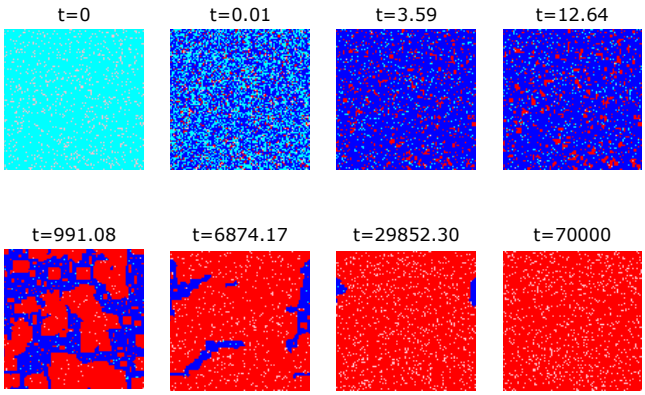

Figure 2. Emergence of a uniform B phase from an A-dominated random mixture of the A and B phases.

	A	B
r^a	0.01	0.01
r^d	1	1
r^c	0.01	100000
n^{tot}	10000	10000

Table 2. Rate constants and total number of enzymes of the two species for the simulation shown in Fig. 2 ($\rho_0' = 10^7$).

By decreasing the $r_B^c \,/\, r_A^c$ ratio, a phase-separated stationary state characterized by phase coexistence is seen to emerge from the initial random mixture via the formation and coarsening of island of the A phase in the sea of the B phase (see Fig. 3 and Table 3).

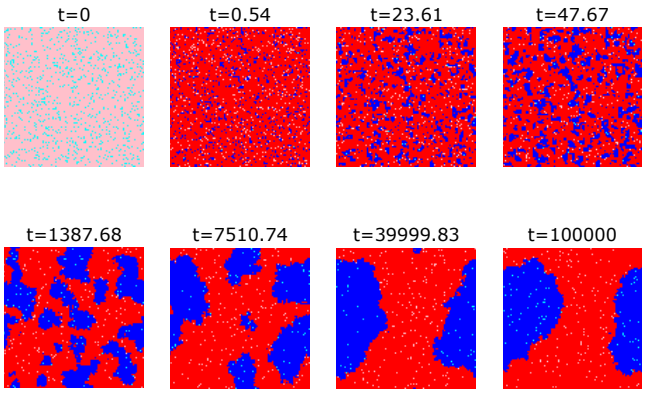

Figure 3. Emergence of a phase coexistence stationary state via the formation and coarsening of island of the A phase in the sea of the B phase.

	A	B
r^a	0.01	0.01
r^d	1	1
r^c	10000	100
n^{tot}	10000	10000

Table 3. Rate constants and total number of enzymes of the two species for the simulation shown in Fig. 3 ($\rho_0' = 10^{-2}$).

By exchanging the parameters for the A and B species one observes a mirror behavior (see Fig. 4).

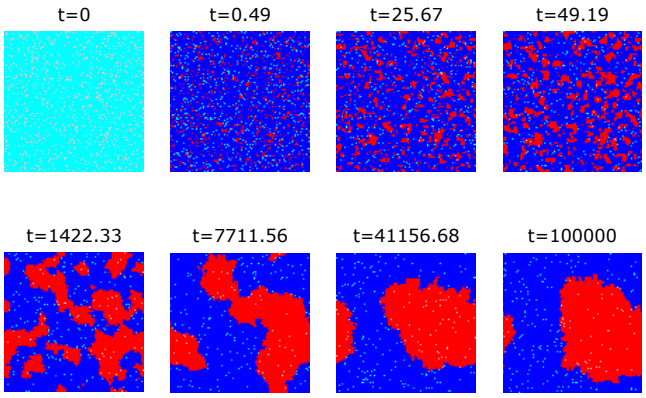

Figure 4. Emergence of a phase coexistence stationary state via the formation and coarsening of island of the B phase in the sea of the A phase.

	A	B
r^a	0.01	0.01
r^d	1	1
r^c	100	10000
n^{tot}	10000	10000

Table 4. Rate constants and total number of enzymes of the two species for the simulation shown in Fig. 4 ($\rho_0' = 10^2$).

3 Slowing down of coarsening in the symmetric case

When $r_B^c \sim r_A^c$, simulations show an effect not predicted by the mean-field theory. Phase separation via coarsening of regions of the A and B phases is significantly slowed down (see Fig. 5 and Table 5). This is likely due to the speed of propagation of fronts of the more favored phase going to zero as $r_B^c / r_A^c \to 1$. This effect is reminiscent of the phenomenology of the two-dimensional voter model where phase ordering with zero surface tension takes place in logarithmic times [8].

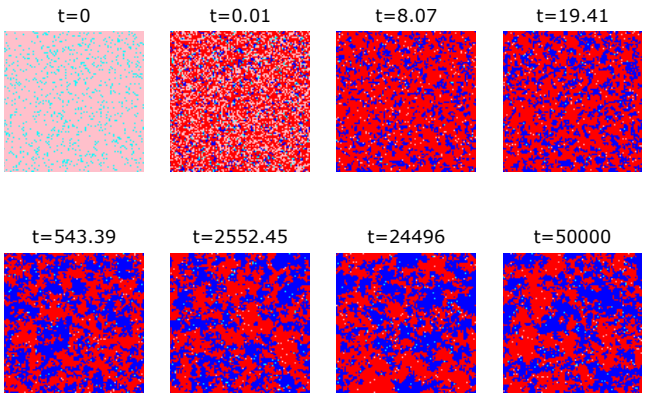

Figure 5. When $r_B^c \sim r_A^c$, phase ordering is slowed down.

	A	B
r^a	0.01	0.01
r^d	1	1
r^c	9000	3000
n^{tot}	10000	10000

Table 5. Rate constants and total number of enzymes of the two species for the simulation shown in Fig. 5 ($\rho_0' = 0.33$).

By exchanging the parameters for the A and B species one observes a mirror behavior (see Fig. 6).

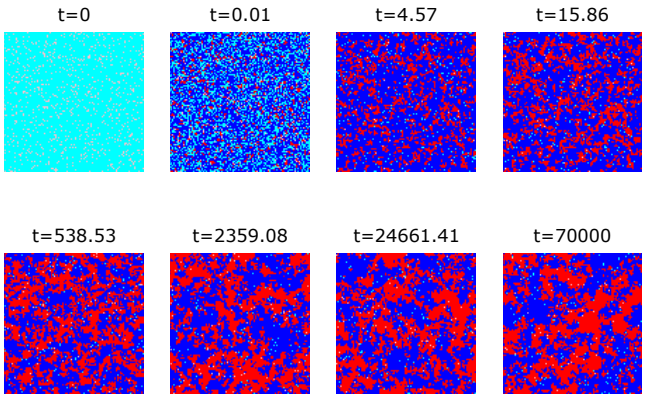

Figure 6. When $r_B^c \sim r_A^c$, phase ordering is slowed down.

	A	B
r^a	0.01	0.01
r^d	1	1
r^c	3000	9000
n^{tot}	10000	10000

Table 6. Rate constants and total number of enzymes of the two species for the simulation shown in Fig. 6 ($\rho_0' = 3$).

The slowing down of phase separation is particularly evident when $r_B^c = r_A^c$ (see Fig. 7 and Table 7).

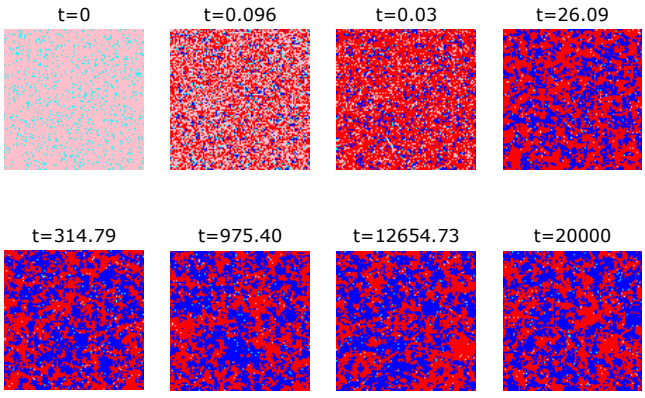

Figure 7. When $r_B^c = r_A^c$, phase ordering is slowed down.

	A	B
r^a	0.01	0.01
r^d	1	1
r^c	10000	10000
$n^{\rm tot}$	10000	10000

Table 7. Rate constants and total number of enzymes of the two species for the simulation shown in Fig. 7 and Fig. 8 ($\rho_0' = 1$).

After initial transient, a similar picture is observed also starting with an A-dominated (10% sites occupied by B molecules) initial configuration (see Fig. 8 and Table 7).

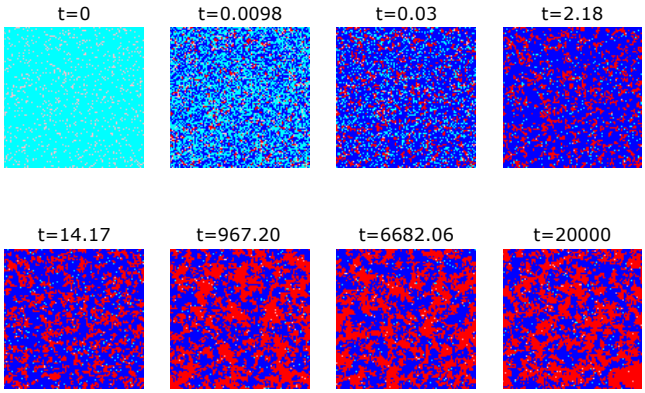

Figure 8. When $r_B^c = r_A^c$, phase ordering is slowed down (A-dominated initial state).

In Fig. 9 typical states for large times are shown for the previously investigated parameter values. The values of ρ_0' grow from left to right, corresponding to large-time states characterized by a uniform A state (leftmost panel), phase coexistence with majority A or B phase, or a uniform B state (rightmost panel). The central panels show typical large-time states for approximately symmetric values of the catalytic rates r_B^c and r_A^c, such that phase separation is slowed down.

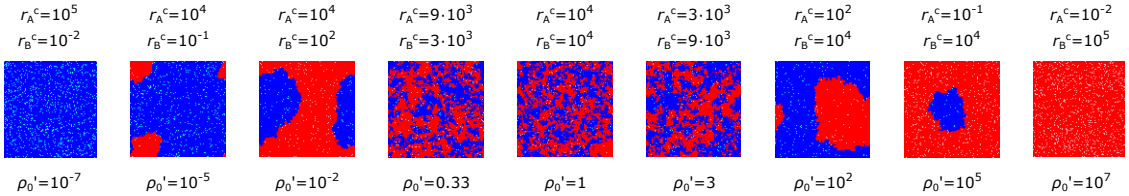

Figure 9. Large-time states corresponding to increasing values of ρ_0' (from left to right).

4 Role of dissociation rates

Here we investigate the role of dissociation rates by performing simulations with the same parameter values as in Tables 3, except for the values of $r_A^d = r_B^d \equiv r^d$, which are here varied. One observes a coarsening scenario similar to the one shown in the previous Figs. 3, 4, but with more irregular interfaces and faster coarsening when r^d is increased (Figs. 10, 11 and corresponding

Tables 8, 9), and with smoother interfaces and slower coarsening when r^d is decreased (Figs. 12, 13 and corresponding Tables 10, 11).

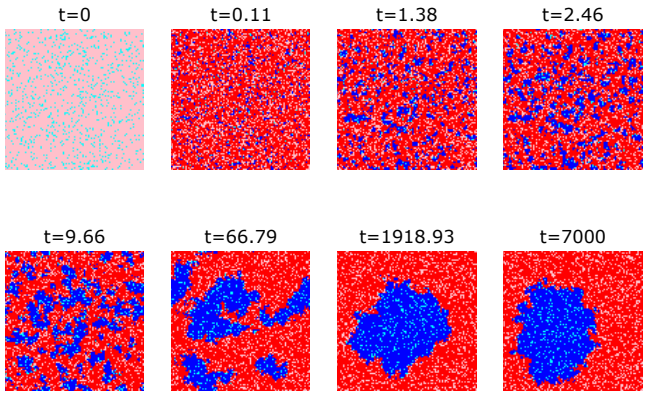

Figure 10. Higher dissociation rates lead to faster coarsening and more irregular interfaces.

	A	B
r^a	0.01	0.01
r^d	10	10
r^c	10000	100
n^{tot}	10000	10000

Table 8. Rate constants and total number of enzymes of the two species for the simulation shown in Fig. 10 ($\rho_0' = 10^{-2}$).

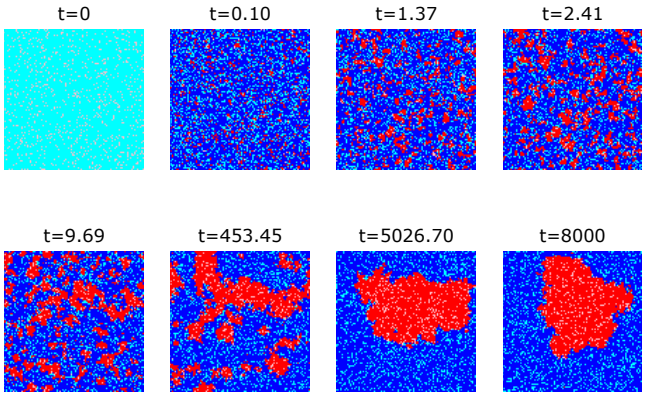

Figure 11. Higher dissociation rates lead to faster coarsening and more irregular interfaces.

	A	B
r^a	0.01	0.01
r^d	10	10
r^c	100	10000
n^{tot}	10000	10000

Table 9. Rate constants and total number of enzymes of the two species for the simulation shown in Fig. 11 ($\rho_0' = 10^2$).

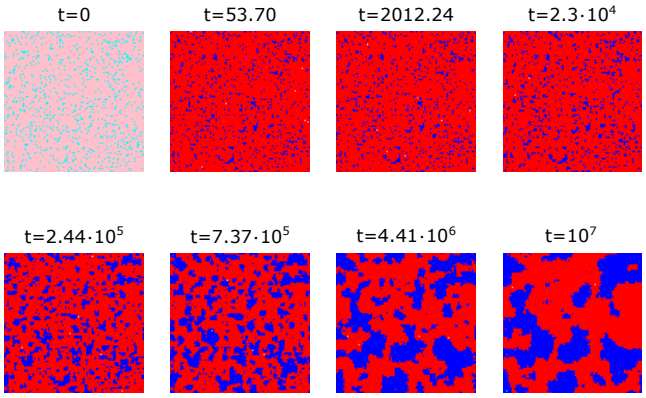

Figure 12. Lower dissociation rates lead to slower coarsening and smoother interfaces.

	A	B
r^a	0.01	0.01
r^d	0.01	0.01
r^c	10000	100
n^{tot}	10000	10000

Table 10. Rate constants and total number of enzymes of the two species for the simulation shown in Fig. 12 ($\rho_0' = 10^{-2}$).

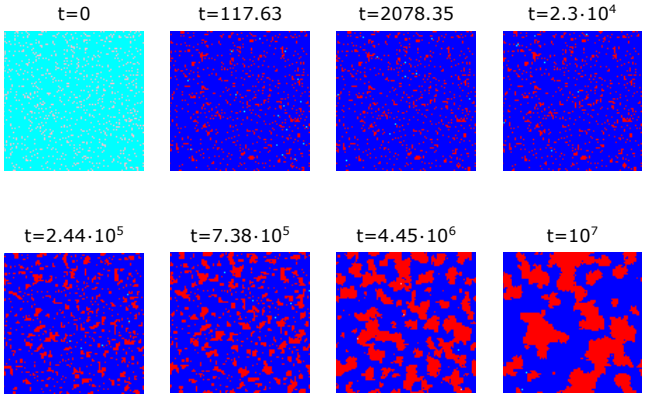

Figure 13. Lower dissociation rates lead to slower coarsening and smoother interfaces.

	A	B
r^a	0.01	0.01
r^d	0.01	0.01
r^c	100	10000
n^{tot}	10000	10000

Table 11. Rate constants and total number of enzymes of the two species for the simulation shown in Fig. 13 ($\rho_0' = 10^{2}$).

We further performed simulations in the completely symmetric case, with the parameter values taken from Table 5, where however the values of $r_A^d = r_B^d \equiv r^d$ are now varied. We observe that a significant coarsening effect cannot be recovered by neither increasing (Fig. 14 and Table 12) nor decreasing r^d (Fig. 15 and Table 13).

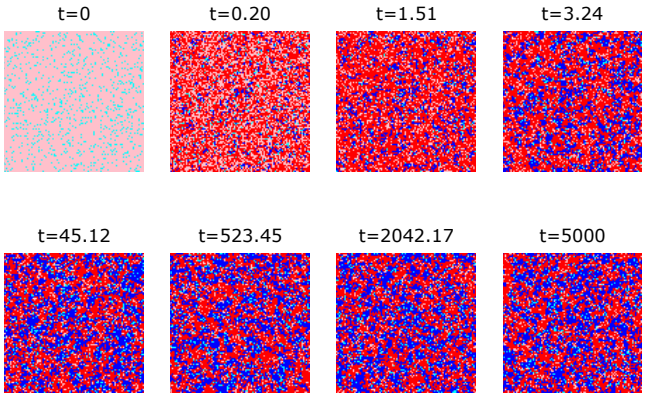

Figure 14. In the completely symmetric case, higher dissociation rates lead to a highly disordered scenario.

	A	B
r^a	0.01	0.01
r^d	10	10
r^c	9000	3000
n^{tot}	10000	10000

Table 12. Rate constants and total number of enzymes of the two species for the simulation shown in Fig. 14 ($\rho_0' = 0.33$).

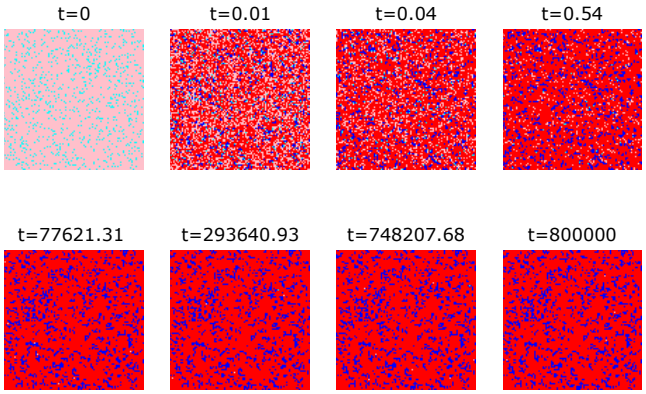

Figure 15. In the completely symmetric case, coarsening is not recovered by lowering dissociation rates.

	A	B
r^a	0.01	0.01
r^d	0.01	0.01
r^c	9000	3000
n^{tot}	10000	10000

Table 13. Rate constants and total number of enzymes of the two species for the simulation shown in Fig. 15 ($\rho_0' = 0.33$).

5 Role of the total number of enzymes

Here we investigate the role of the total number of enzymes by performing simulations with the same parameter values as in Table. 1, except for the values of n_A^{tot} and n_B^{tot}, which are here varied.

By increasing n_A^{tot} or n_B^{tot} (Figs. 16–19 and corresponding Tables 14–17) we observe that the phase coexistence region shrinks (compare e.g. Fig. 3 and Table 3 with Fig. 18 and Table 16). Moreover, high values of n_A^{tot} and/or n_B^{tot} favor the relaxation to absorbing states (Figs. 16–19).

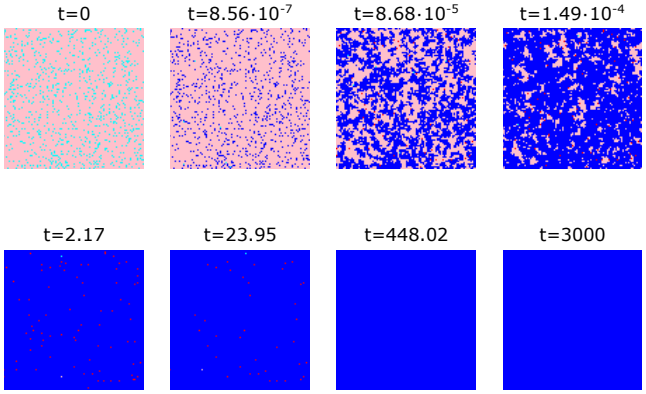

Figure 16. A high total number of enzymes favors the relaxation to absorbing states.

	A	B
r^a	0.01	0.01
r^d	1	1
r^c	10000	10000
n^{tot}	10^{11}	10000

Table 14. Rate constants and total number of enzymes of the two species for the simulation shown in Fig. 16 ($\rho_0' = 10^{-7}$).

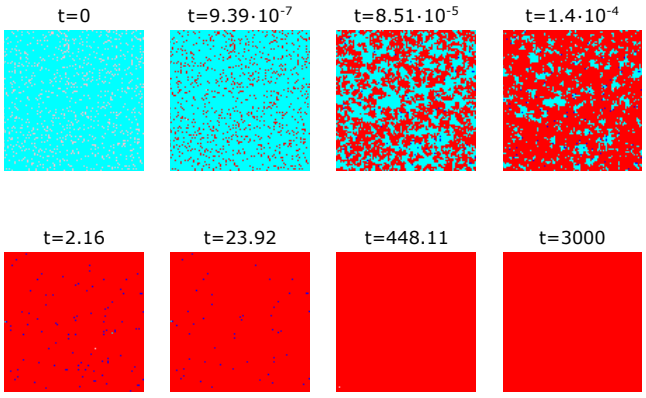

Figure 17. A high total number of enzymes favors the relaxation to absorbing states.

	A	B
r^a	0.01	0.01
r^d	1	1
r^c	10000	10000
n^{tot}	10000	10^{11}

Table 15. Rate constants and total number of enzymes of the two species for the simulation shown in Fig. 17 ($\rho_0' = 10^{7}$).

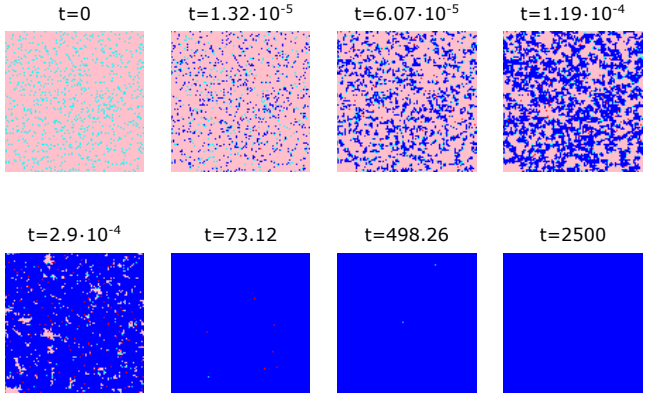

Figure 18. Increasing the total number of the enzymes leads to the disappearance of the phase-separated stationary state (compare with Fig. 3).

	A	B
r^a	0.01	0.01
r^d	1	1
r^c	10000	10000
n^{tot}	10^6	10000

Table 16. Rate constants and total number of enzymes of the two species for the simulation shown in Fig. 18 ($\rho_0' = 10^{-2}$).

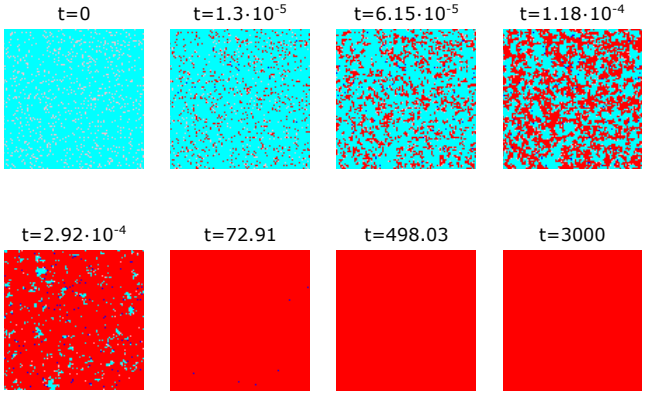

Figure 19. Increasing the total number of the enzymes leads to the disappearance of the phase-separated stationary state (compare with Fig. 4).

	A	B
r^a	0.01	0.01
r^d	1	1
r^c	10000	10000
n^{tot}	10000	10^6

Table 17. Rate constants and total number of enzymes of the two species for the simulation shown in Fig. 19 ($\rho_0' = 10^2$).

Decreasing the total number of enzymes below the number of lattice sites (Figs. 20–23 and corresponding Tables 18–21), we observed more irregular interfaces and faster coarsening, similarly to what previously seen by increasing the dissociation rate (see Figs. 10, 11 and corresponding

Tables 8, 9). Actually, by either decreasing the total number of enzymes, or by increasing their dissociation rate, one similarly gets less membrane-bound enzymes (of the order of 90% of the sites in the simulations of Figs. 20–23), with the apparent effect of destabilizing the phase-separated regions.

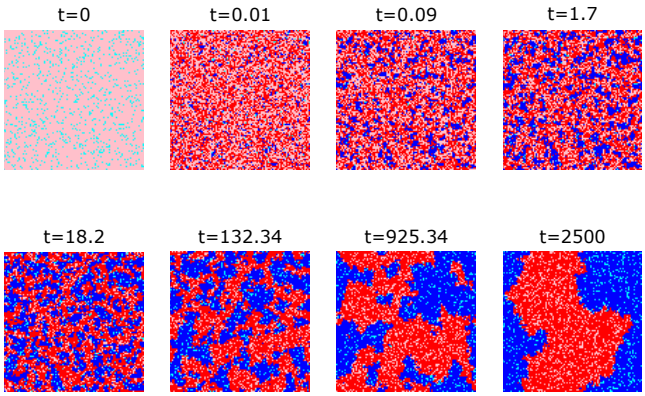

Figure 20. Lowering the total number of enzymes leads to faster coarsening and more irregular interfaces.

	A	B
r^a	0.01	0.01
r^d	1	1
r^c	10000	100
n^{tot}	4750	4750

Table 18. Rate constants and total number of enzymes of the two species for the simulation shown in Fig. 20 ($\rho_0' = 10^{-2}$).

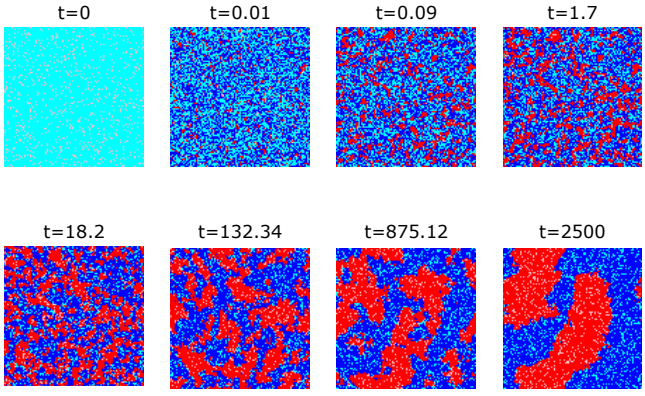

Figure 21. Lowering the total number of enzymes leads to faster coarsening and more irregular interfaces.

	A	B
r^a	0.01	0.01
r^d	1	1
r^c	100	10000
n^{tot}	4750	4750

Table 19. Rate constants and total number of enzymes of the two species for the simulation shown in Fig. 21 ($\rho_0' = 10^{2}$).

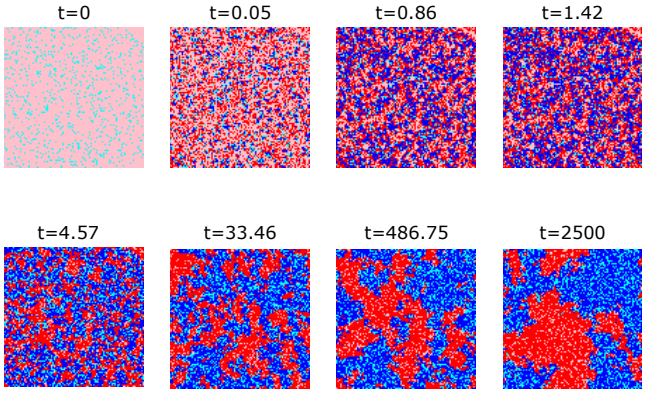

Figure 22. Further lowering the total number of enzymes leads to even faster coarsening and more irregular interfaces.

	A	B
r^a	0.01	0.01
r^d	1	1
r^c	10000	100
n^{tot}	4156	4156

Table 20. Rate constants and total number of enzymes of the two species for the simulation shown in Fig. 22 ($\rho_0' = 10^{-2}$).

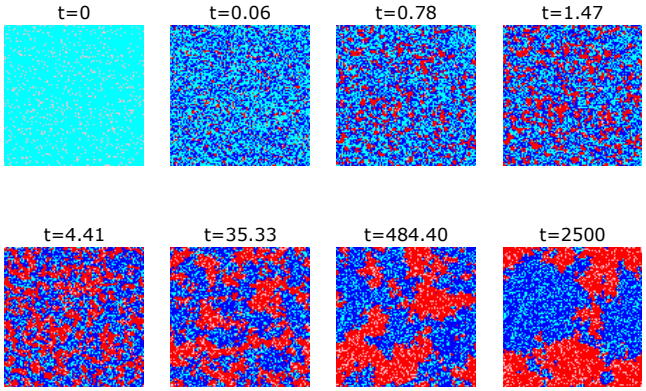

Figure 23. Further lowering the total number of enzymes leads to even faster coarsening and more irregular interfaces.

	A	B
r^a	0.01	0.01
r^d	1	1
r^c	100	10000
n^{tot}	4156	4156

Table 21. Rate constants and total number of enzymes of the two species for the simulation shown in Fig. 23 ($\rho_0' = 10^2$).

With the present set of parameter values, when the fraction of membrane-bound enzymes becomes less than approximately 75% of the sites (Figs. 24, 25 and corresponding Tables 22, 23), the coarsening process is impaired and highly disordered configurations take the place of the previously observed ordered, phase-separated states.

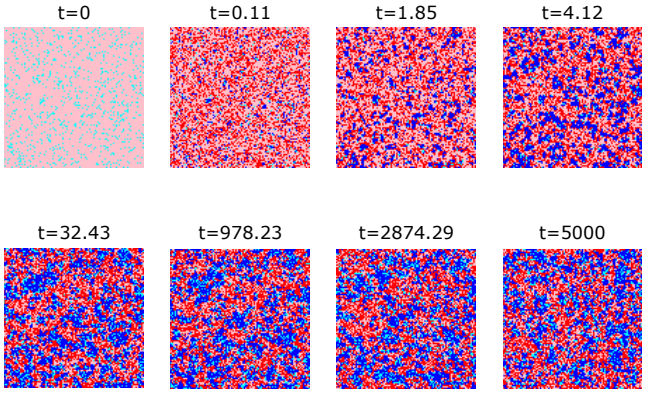

Figure 24. With the present set of parameters, when the fraction of membrane-bound enzymes drops below 75%, the phase ordering process is significantly impaired.

	A	B
r^a	0.01	0.01
r^d	1	1
r^c	10000	100
n^{tot}	3562	3562

Table 22. Rate constants and total number of enzymes of the two species for the simulation shown in Fig. 24 ($\rho_0' = 10^{-2}$).

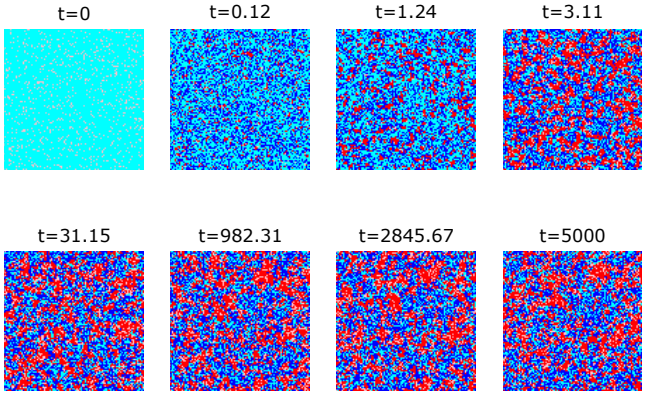

Figure 25. With the present set of parameters, when the fraction of membrane-bound enzymes drops below 75%, the phase ordering process is significantly impaired.

	A	B
r^a	0.01	0.01
r^d	1	1
r^c	100	10000
n^{tot}	3562	3562

Table 23. Rate constants and total number of enzymes of the two species for the simulation shown in Fig. 25 ($\rho_0' = 10^{2}$).

Conclusions

In this thesis, we studied a simplified model of active phase separation on cell membranes based on the competing enzymatic activity of two molecular species by both a mean-field approach and numerical simulations. We derived a mean-field phase diagram identifying parameter regions where the membrane system tends to demix by either a nucleation process or by spinodal decomposition. This analytical approach led to an interesting prediction: in the presence of comparable surface concentrations of membrane-bound molecules, phase separation is expected to be favored on larger membrane bodies. Moreover, we found that, in the framework of the mean-field model, a necessary condition for the appearance of phase-separated states via a nucleation process is that enzymatic action takes place in the saturation regime of Michaelis-Menten kinetics. Numerical simulations confirmed the qualitative structure of the mean-field diagram and highlighted an interesting kinetic effect that the mean-field approach could not capture: in the symmetric case, when the kinetic rates of the two molecular species became approximately equal, the phase separation process was impaired and the system did not demix. We also observed that lowering the number of membrane-bound enzymes led to rougher interfaces and faster coarsening, and to the almost complete disappearance of coarsening below some threshold. It would be quite interesting to further investigate these fluctuation-induced phenomena by going beyond the mean-field approach.

Appendix A

We provide here for convenience the derivation of the Michaelis-Menten expression for enzymatic kinetics. One assumes that an enzyme E forms a transient bound state $E\,S$ with a "substrate" S, which, by the enzymatic action of E, can be transformed into the product P:

$$[E]+[S] \underset{k^a}{\overset{k^d}{\leftrightarrows}} [E\,S] \overset{k^c}{\rightarrow} [E]+[P] \tag{A.1}$$

where the square brackets denote concentrations of the molecular factors and k^a, k^d and k^c are kinetic constants. The kinetic equations for the system of reactions (A.1) are

$$\frac{\partial[E\,S]}{\partial t} = k^a[E]\,[S]-k^d[E\,S]-k^c[E\,S] \tag{A.2}$$

$$\frac{\partial[P]}{\partial t} = k^c[E\,S] \tag{A.3}$$

Assuming now that:

– the reactions are in an approximately stationary state, so that:

$$\begin{aligned}[E\,S] &= k^a\,[E]\,[S]\,/\,(k^c+k^d)\\ [E\,S] &= [E]\,[S]\,/\,K\end{aligned} \tag{A.4}$$

where

$$K=\frac{k^c+k^d}{k^a}$$

is the Michaelis-Menten constant;

– the number of enzymes E is much smaller than that of the substrates S, so that:

$$[S] = [S_{\rm tot}]-[E\,S] \simeq [S_{\rm tot}] \tag{A.5}$$

$$[E] = [E_{\rm tot}]-[E\,S] \tag{A.6}$$

from (A.4) we get

$$[E\,S] = \frac{[E_{\rm tot}]\,[S_{\rm tot}]}{K+[S_{\rm tot}]}$$

and also

$$\frac{\partial[P]}{\partial t}=k^c\,[E_{\rm tot}]\,\frac{[S_{\rm tot}]}{K+[S_{\rm tot}]}$$

which is the Michaelis-Menten equation for the speed of the catalytic reaction. When $[S_{\rm tot}]$ tends to infinity we get

$$v_{\rm max}=k^c\,[E_{\rm tot}]$$

which is the maximum velocity of the catalytic reaction in the saturation regime.

Bibliography

[1] Anthony A. Hyman, Christoph A. Weber, and Frank Jülicher. Liquid-liquid phase separation in biology. *Annual Review of Cell and Developmental Biology*, 30:39–58, 2014.

[2] Joel Berry, Clifford P Brangwynne, and Mikko Haataja. Physical principles of intracellular organization via active and passive phase transitions. *Reports on Progress in Physics*, 81:046601, 2018.

[3] Salman F. Banani, Hyun O. Lee, Anthony A. Hyman, and Michael K. Rosen. Biomolecular condensates: organizers of cellular biochemistry. *Nature Reviews Molecular Cell Biology*, 18:285–298, 2017.

[4] Elisa Floris, Andrea Piras, Luca Dall'Asta, Andrea Gamba, Emilio Hirsch, and Carlo C. Campa. Physics of compartmentalization: How phase separation and signaling shape membrane and organelle identity. *Computational and Structural Biotechnology Journal*, 19:3225, 2021.

[5] Andrea Gamba, Antonio De Candia, Stefano Di Talia, Antonio Coniglio, Federico Bussolino, and Guido Serini. Diffusion-limited phase separation in eukaryotic chemotaxis. *Proceedings of the National Academy of Sciences*, 102:16927–16932, 2005.

[6] Matteo Semplice, Andrea Veglio, Giovanni Naldi, Guido Serini, and Andrea Gamba. A bistable model of cell polarity. *PloS one*, 7:30977, 2012.

[7] Daniel T. Gillespie. Exact stochastic simulation of coupled chemical reactions. *The Journal of Physical Chemistry*, 81:2340, 1977.

[8] Ivan Dornic, Hugues Chaté, Jérôme Chave, and Haye Hinrichsen. Critical coarsening without surface tension: The universality class of the voter model. *Physical Review Letters*, 87:045701, 2001.